Supporting Information for: Electronic Exciton–Plasmon Coupling in a Nanocavity Beyond the Electromagnetic Interaction Picture

Antton Babaze,[*,†,‡] Ruben Esteban,[†,¶,‡] Andrei G. Borisov,[§] and Javier Aizpurua[*,†,‡]

†*Materials Physics Center CSIC-UPV/EHU, Paseo Manuel de Lardizabal 5 20018, Donostia-San Sebastián, Spain*

‡*Donostia International Physics Center DIPC, Paseo Manuel de Lardizabal 4 20018, Donostia-San Sebastián, Spain*

¶*IKERBASQUE, Basque Foundation for Science, 48013 Bilbao, Spain*

§*Institut des Sciences Moléculaires d'Orsay, UMR 8214 CNRS-Université Paris-Saclay, Bât. 520, 91405 Orsay Cedex, France*

E-mail: anttonbabaze@dipc.org; aizpurua@ehu.eus

Contents

S1 Characterization of the Model Quantum Emitter (QE)

In this section, we explain the approach to model the quantum emitter (QE) considered in the quantum calculations. The ground-state properties of the isolated QE are determined using the density functional theory (DFT), and the excitation of the QE by an external perturbation is described using the time-dependent density functional theory (TDDFT) framework. The electronic structure of the QE is addressed within the free-electron jellium model, in a similar way as we model the metallic nanoparticles. We consider a spherical QE of radius R_{qe} containing two valence electrons. The spin-restricted case is considered.[1] In the ground-state configuration of the QE, the total spin is zero, and the 2 electrons with opposite spins occupy the same Kohn–Sham (KS) valence orbital. From the charge neutrality condition, the positive background density n_+ representing the atomic cores of the QE and spreading over its spatial extent satisfies

$$\frac{4}{3}\pi R_{\mathrm{qe}}^3 n_+ = 2. \tag{S1}$$

Throughout this Supporting Information atomic units (au) are used unless otherwise stated.

S1.1 Ground-state properties of the isolated QE

The occupied and unoccupied one-electron KS orbitals $\Psi^0_{\mathrm{qe},j}(\mathbf{r})$ of the QE, with $j = 1, 2, 3, 4, \ldots$ referring to the occupied ($j = 1$) and onuccupied ($j = 2, 3, 4, \ldots$) orbitals, and their energies $\epsilon_{\mathrm{qe},j}$ are obtained from the static KS equations of DFT that depend on the ground-state density $n^0_{\mathrm{qe}}(\mathbf{r})$,

$$\begin{aligned} \hat{H}[n^0_{\mathrm{qe}}]\Psi^0_{\mathrm{qe},j}(\mathbf{r}) &= \epsilon_{\mathrm{qe},j}\Psi^0_{\mathrm{qe},j}(\mathbf{r}), \\ \hat{H}[n^0_{\mathrm{qe}}] &= \hat{T} + V_{\mathrm{h}}[n^0_{\mathrm{qe}}](\mathbf{r}) + V_{\mathrm{xc}}[n^0_{\mathrm{qe}}](\mathbf{r}) + V_{\mathrm{qe}}(\mathbf{r}), \end{aligned} \tag{S2}$$

where $\hat{T}$, $V_{\rm h}[n^0_{\rm qe}](\mathbf{r})$ and $V_{\rm xc}[n^0_{\rm qe}](\mathbf{r})$ are the kinetic energy operator, the Hartree potential and the exchange–correlation potential, respectively, calculated within the adiabatic local-density approximation (ALDA) following a self-consistent procedure.[2]

$V_{\rm qe}(\mathbf{r})$ in Equation S2 is an attractive potential introduced along the lines of the so-called stabilized jellium model.[3] It is localized in the spatial region of the QE,

$$V_{\rm qe}(\mathbf{r}) = -V_0 e^{-4|\mathbf{r}|^2/R^2_{\rm qe}}, \tag{S3}$$

and allows us to control the one-electron energy levels $\epsilon_{{\rm qe},j}$ of the QE states by changing the parameters V_0 and $R_{\rm qe}$.

As mentioned above, the spin-restricted ground state of the two-electron spherical QE is characterized by the doubly-occupied KS orbital, $\Psi^0_{{\rm qe},1}(\mathbf{r})$, resulting in an electron density

$$n^0_{\rm qe}(\mathbf{r}) = 2|\Psi^0_{{\rm qe},1}(\mathbf{r})|^2. \tag{S4}$$

In the main text, we refer to $\Psi^0_{{\rm qe},1}(\mathbf{r})$ as the *highest occupied molecular orbital* (HOMO), which is a $1s(\ell = 0, m = 0)$ orbital with zero orbital (ℓ) and magnetic (m) quantum numbers. Thus, the electronic configuration of the QE is $1s^2$. The energy level of the HOMO state is $\mathrm{E}_{\rm homo} = \epsilon_{{\rm qe},1}$.

For the values of V_0 and $R_{\rm qe}$ (Equation S3) considered in this work, we find only three energy-degenerate excited KS orbitals accessible for optical transitions from the ground state. These orbitals correspond to the $2p$-shell and are characterized by the orbital momentum $\ell = 1$ and magnetic quantum numbers $m = 0, \pm 1$. With $\psi_{2p}(r)$ the radial part of the wave function, we can define

$$\begin{aligned}
\Psi^0_{{\rm qe},2}(\mathbf{r}) &= Y^0_1(\theta,\varphi)\psi_{2p}(r),\\
\Psi^0_{{\rm qe},3}(\mathbf{r}) &= Y^{-1}_1(\theta,\varphi)\psi_{2p}(r),\\
\Psi^0_{{\rm qe},4}(\mathbf{r}) &= Y^1_1(\theta,\varphi)\psi_{2p}(r),
\end{aligned} \tag{S5}$$

where $Y_\ell^m(\theta,\varphi)$ are the spherical harmonics. Because of the symmetry of the system considered in the main text, for an incident electromagnetic wave polarized along the z-axis, the electronic transitions are effective between the ground-state 1s KS orbital and the $2p(\ell=1, m=0)$ KS orbital with wave function $\Psi^0_{\mathrm{qe},2}(\mathbf{r})$. For the sake of simplicity, in the main text we refer to $\Psi^0_{\mathrm{qe},2}(\mathbf{r})$ as the *lowest unoccupied molecular orbital* (LUMO).

The free parameters V_0 and R_{qe} are used to determine the energy levels of the HOMO ($\mathrm{E_{homo}} = \epsilon_{\mathrm{qe},1}$) and the LUMO ($\mathrm{E_{lumo}} = \epsilon_{\mathrm{qe},2}$) of the QE. As a consequence, these parameters determine the oscillator strength α_0 and resonant frequency ω_0 of the QE exciton, as explained in Subsection S1.2.

The $\mathrm{E_{homo}}$ and $\mathrm{E_{lumo}}$ energy levels obtained for different values of the background potential $V_0 = 1$ eV, 3 eV, 5 eV, 7 eV and QE radius $R_{\mathrm{qe}} = 3.8$ $\mathrm{a_0}$, 5 $\mathrm{a_0}$, 6.3 $\mathrm{a_0}$ are shown in Table S1. The case of $V_0 = 1$ eV and $R_{\mathrm{qe}} = 5$ $\mathrm{a_0}$ corresponds to the QE considered in Figures $1-4$ of the main text, while $V_0 = 5$ eV and $R_{\mathrm{qe}} = 5$ $\mathrm{a_0}$ are used to obtain the results in Figure 5. The results shown in the rest of this Supporting Information are obtained for $R_{\mathrm{qe}} = 5$ $\mathrm{a_0}$ unless otherwise stated.

Table S1: Energy levels of the HOMO ($\mathrm{E_{homo}}$) and the LUMO ($\mathrm{E_{lumo}}$) of the isolated QE as obtained from static DFT calculations for different values of V_0 and R_{qe}, together with the oscillator strength α_0 and resonant frequency ω_0 obtained by fitting the classical polarizability to the TDDFT results according to Equation S8. All the energies are given in electronvolts (eV), while the values of α_0 are given in atomic units (au).

	$\mathbf{R_{qe}}$ = 3.8 $\mathbf{a_0}$				**$\mathbf{R_{qe}}$ = 5 $\mathbf{a_0}$**				**$\mathbf{R_{qe}}$ = 6.3 $\mathbf{a_0}$**			
	$\mathrm{E_{homo}}$	$\mathrm{E_{lumo}}$	ω_0	α_0	$\mathrm{E_{homo}}$	$\mathrm{E_{lumo}}$	ω_0	α_0	$\mathrm{E_{homo}}$	$\mathrm{E_{lumo}}$	ω_0	α_0
$\mathbf{V_0}$ = 1 eV	-4.03	-1.10	3.45	1.50	-3.29	-1.23	2.58	1.70	-2.79	-1.25	2.02	1.79
$\mathbf{V_0}$ = 3 eV	-4.13	-1.04	3.60	1.43	-3.4	-1.16	2.75	1.62	-2.92	-1.17	2.20	1.70
$\mathbf{V_0}$ = 5 eV	-4.26	-0.97	3.76	1.35	-3.57	-1.08	2.95	1.52	-3.10	-1.11	2.43	1.61
$\mathbf{V_0}$ = 7 eV	-4.40	-0.90	3.94	1.30	-3.75	-1.02	3.18	1.45	-3.33	-1.06	2.70	1.54

S1.2 Optical response of the isolated QE

In order to obtain the optical response of the isolated QE, we use real-time TDDFT simulations of its linear response as implemented in refs. 2,4–6, and calculate the dynamics of the z-component of the induced dipole moment $p_{\mathrm{qe}}(t) = -\int_V d^3\mathbf{r}\, z\, [n_{\mathrm{qe}}(\mathbf{r},t) - n^0_{\mathrm{qe}}(\mathbf{r})]$

in response to an external impulsive perturbation with electric field $E_\delta(t) = \mathrm{E}_0 \Delta t\ \delta(t)$ polarized along the z-axis.[7] Here $\mathrm{E}_0 = 10^{-5}$ au and $\Delta t = 0.05$ au are the amplitude of the perturbation and the time-step used in the propagation, respectively, and $\delta(t)$ is the Dirac delta function. The x and y components of the induced dipole moment are zero because of the symmetry. The integral extends over the whole volume V and the electron density $n_{\mathrm{qe}}(\mathbf{r}, t)$ evolves in time due to the external perturbation, departing from its initial ground-state value, $n_{\mathrm{qe}}(\mathbf{r}, t = 0) = n^0_{\mathrm{qe}}(\mathbf{r})$.

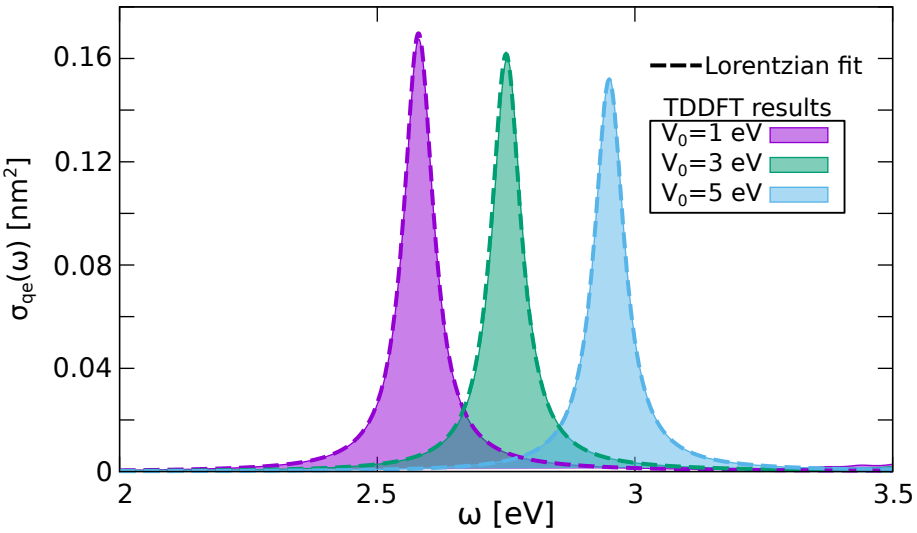

Figure S1: Absorption cross-section of the isolated QE with radius $R_{\mathrm{qe}} = 5\ \mathrm{a}_0$, as obtained from TDDFT simulations for different values of the parameter V_0 in Equations S3 (filled curves). Results are shown as a function of the frequency ω of the incoming linearly-polarized electromagnetic plane wave. The dashed lines correspond to the absorption of the QE obtained by fitting the classical polarizability given by Equation S8 to the TDDFT results. The parameters α_0 (oscillator strength) and ω_0 (resonant frequency of the QE) resulting from this fit are given in Table S1. An intrinsic damping $\gamma_{\mathrm{qe}} = 70$ meV is used.

The frequency-resolved absorption cross-section $\sigma_{\mathrm{qe}}(\omega)$ of the isolated QE,

$$\sigma_{\mathrm{qe}}(\omega) = \frac{4\pi\omega}{c}\mathrm{Im}\{\alpha_{\mathrm{qe}}(\omega)\}, \tag{S6}$$

(c is the speed of light) can be obtained from the TDDFT calculations of the QE polarizability $\alpha_{\mathrm{qe}}(\omega)$ according to

$$\alpha_{\mathrm{qe}}(\omega) = \alpha^{\mathrm{tddft}}_{\mathrm{qe}}(\omega) = -\frac{1}{\mathrm{E}_0\ \Delta t}\int_0^{T_f} dt\ p_{\mathrm{qe}}(t) e^{i(\omega + i\eta/2)t}, \tag{S7}$$

where the propagation time-step $\Delta t = 0.05$ au and final propagation time $T_f = 4000$ au are used in our simulations, which we have checked is enough to achieve convergence. The attenuation parameter $\eta = 70$ meV is set equal to that used for the total QE–MNPs system (see Subsection S2.1). It corresponds to the decay rate of the QE in vacuum. It should be noted however that, for the QE interacting with the dimer antenna, the decay rate of the exciton is not only determined by this "intrinsic" broadening, but also by the Ohmic losses in metal nanoparticles.[8,9]

Figure S1 shows the absorption cross section $\sigma_{\mathrm{qe}}(\omega)$ of the isolated QE as obtained from TDDFT calculations (filled curves) for QE radius $R_{\mathrm{qe}} = 5$ a$_0$ and several values of the background potential, $V_0 = 1$ eV, 3 eV and 5 eV (Equation S3).

The frequency dependence of the cross section obtained with the TDDFT calculations (filled curves in Figure S1) can be fitted with a classical resonance profile (dashed lines in Figure S1)

$$\alpha_{\mathrm{qe}}(\omega) = \alpha_{\mathrm{qe}}^{\mathrm{classical}}(\omega) = \frac{\alpha_0}{\left(\omega_0^2 - \omega^2 - i\omega\gamma_{\mathrm{qe}}\right)}, \tag{S8}$$

allowing to determine the oscillator strength α_0, the resonant frequency ω_0 and the decay rate γ_{qe} of the isolated QE. The ω_0 and α_0 parameters obtained for the three values of V_0 considered in Figure S1 are reported in Table S1, where we also provide the corresponding results obtained for different radii of the QE, $R_{\mathrm{qe}} = 3.8$ a$_0$ and $R_{\mathrm{qe}} = 6.3$ a$_0$. In all cases, $\gamma_{\mathrm{qe}} = 70$ meV, given by the attenuation parameter η used in Equation S7. The values of α_0 and ω_0 calculated for the QE with $V_0 = 1$ eV and $R_{\mathrm{qe}} = 5$ a$_0$ are used to obtain the results shown in Figures 1d and 2a of the main text.

As shown in Table S1, the resonant energy ω_0 of the electronic transition in the QE does not match exactly the energy difference between the one-electron energy levels obtained from static DFT calculations, i.e., $\omega_0 \neq \mathrm{E_{lumo}} - \mathrm{E_{homo}}$. Indeed, according to the Kohn–Sham scheme of TDDFT adopted in this work, $\mathrm{E_{homo}}$ and $\mathrm{E_{lumo}}$ represent the energy levels of a fictitious non-interacting electron system, so that the resonant energies of the interacting system will be renormalized with respect to the non-interacting one *via*

Coulomb and exchange–correlation potentials.[10,11]

S2 Quantum Description of a QE–MNPs System

S2.1 Optoelectronic response of the hybrid QE–MNP system within TDDFT

The occupied ground-state KS orbitals $\psi_j^0(\mathbf{r})$ of the coupled QE–MNPs system are obtained within the TDDFT procedure starting from the KS orbitals of the individual constituents and adiabatically reducing the interparticle distance so that the sought geometry is reached, as described in detail in ref. 2. These ground-state occupied KS orbitals of the total system are used as initial states in the TDDFT time propagation, $\psi_j(\mathbf{r}, t=0) = \psi_j^0(\mathbf{r})$, to determine the electron-density evolution $n(\mathbf{r}, t) = \sum_j |\psi_j(\mathbf{r}, t)|^2$ in response to an external weak excitation of amplitude E_0 applied at the instant of time $t = 0$.

The dynamics of the electron density $n(\mathbf{r}, t)$ of the total QE–MNPs hybrid is obtained from the time-dependent KS equations,

$$\begin{aligned} i\frac{\partial}{\partial t}\psi_j(\mathbf{r}, t) &= \{\hat{T} + V_{\mathrm{tot}}[n](\mathbf{r}, t)\}\psi_j(\mathbf{r}, t), \\ V_{\mathrm{tot}}[n](\mathbf{r}, t) &= V_{\mathrm{h}}[n](\mathbf{r}, t) + V_{\mathrm{xc}}[n](\mathbf{r}, t) + V_{\mathrm{qe}}(\mathbf{r}), \end{aligned} \tag{S9}$$

where $\psi_j(\mathbf{r}, t)$ are the occupied KS orbitals that evolve in time in response to an external (weak) perturbation.[7] In Equation S9, $\hat{T}$ is the kinetic-energy operator, $V_{\mathrm{h}}[n](\mathbf{r}, t)$ is the Hartree potential, $V_{\mathrm{xc}}[n](\mathbf{r}, t)$ is the exchange–correlation potential calculated within the adiabatic local-density approximation[12,13] (ALDA) using the kernel of Gunnarsson and Lundqvist,[14] and $V_{\mathrm{qe}}(\mathbf{r})$ is the attractive potential localized in the spatial region of the QE given by Equation S3. See reference 2 for further details on the numerical method used to solve Equation S9.

The polarizability of the total system, $\alpha(\omega)$, is obtained from the Fourier transform of

the induced dipole moment $p(t)$ according to

$$\alpha(\omega) = -\frac{1}{\mathrm{E}_0\,\Delta t}\int dt\; p(t)e^{i\omega t-\eta/2t}, \tag{S10}$$

where $\mathrm{E}_0 = 10^{-5}$ au is the amplitude of the external perturbation, $\Delta t = 0.05$ au is the time step used in our simulation, and $\eta = 70$ meV accounts for dissipation processes that are not included in the adopted TDDFT scheme. The absorption spectra are calculated from $\sigma_{\mathrm{abs}}(\omega) = \frac{4\pi\omega}{c}\mathrm{Im}\{\alpha(\omega)\}$, with c the speed of light.

S2.2 Projected density of electronic states (PDOS)

As explained in the previous subsection S2.1, to obtain the optical response of the QE–MNPS system we only propagate the occupied KS orbitals $\psi_j(\mathbf{r}, t)$, and thus we have *a priori* no information about the *unoccupied* electronic states relevant for the discussion of the transfer of an excited electron between the QE and the MNPs. To access the energies of both the occupied and unoccupied KS one-electron states of the coupled QE–MNPs system we calculate the projected density of electronic states (PDOS).

The PDOS represents the number of one-electron states of a particular spatial symmetry that the coupled QE–MNPs system sustains at a given energy level and spatial region. This PDOS includes the contribution of both the occupied and the unoccupied states, and it gives information about the degree of localization of a particular electronic state at a certain spatial region. Notice that since the PDOS shows the one-electron energy states available in a (fictitious) non-interacting Kohn–Sham electron system, the true resonant energies of the coupled QE–MNPs system will also be renormalized as discussed in Subsection S1.2. However, the PDOS still provides insights into the level of electronic hybridization of the occupied and unoccupied states in the coupled QE–MNPs system, and thus, it is a valuable tool to analyze the effects of the electronic QE–MNPs coupling discussed in this work.

In order to calculate the PDOS $\Sigma(\omega)$ in the coupled QE–MNPs system, we use the method of Wave-Packet Propagation.[15] We choose an initial wave packet $\psi(\mathbf{r}, t = 0) = \psi_0(\mathbf{r})$ of a particular symmetry and propagate it according to the time-dependent Schrödinger equation for an effective Hamiltonian $\hat{H}$. This (time-independent) Hamiltonian $\hat{H} = \hat{T} + V_{\text{tot}}(\mathbf{r})$ describes an electron evolving in the ground-state potential $V_{\text{tot}}(\mathbf{r}) = V_{\text{tot}}[n](\mathbf{r}, t = 0)$ of the QE–MNPs structure given by Equation S9. The time evolution of the initial wave packet is thus obtained from

$$\psi(\mathbf{r}, t) = e^{-i\hat{H}\,t}\psi_0(\mathbf{r}) \tag{S11}$$

using the same short-time propagation algorithm as in the TDDFT solution of the time-dependent KS equations of the total QE–MNPs system.[2]

From the time-to-energy Laplace transform $\hat{\mathcal{L}}_\omega$ of the time-dependent wave packet $\psi(\mathbf{r}, t)$ we obtain

$$\hat{\mathcal{L}}_\omega\psi(\mathbf{r}, t) = \int_0^\infty dt\; e^{i(\omega+i\zeta)t}\psi(\mathbf{r}, t) = \int_0^\infty dt\; e^{i(\omega-\hat{H}+i\zeta)t}\psi_0(\mathbf{r}) = \frac{i}{(\omega - \hat{H} + i\zeta)}\psi_0(\mathbf{r}), \tag{S12}$$

where ζ is a small real number.

Expanding the initial wave-packet $\psi_0(\mathbf{r})$ in the eigenfunctions $\Phi_j(\mathbf{r})$ of $\hat{H}$, the Laplace transform of $\psi(\mathbf{r}, t)$ reads

$$\hat{\mathcal{L}}_\omega\psi(\mathbf{r}, t) = i\sum_{j=1}^{\infty}\frac{c_j\Phi_j(r)}{(\omega - \epsilon_j + i\zeta)}, \tag{S13}$$

where ϵ_j are the eigenergies of the Hamiltonian $\hat{H}$ and the complex coefficients c_j are obtained from

$$c_j = \langle\Phi_j(\mathbf{r})|\psi_0(\mathbf{r})\rangle. \tag{S14}$$

Finally, projecting Equation S13 on the initial wave-packet one obtains

$$\langle \psi_0(\mathbf{r}) | \hat{\mathcal{L}}_\omega \psi(\mathbf{r},t) \rangle = i \sum_{j=1}^{\infty} \frac{|c_j|^2}{(\omega - \epsilon_j + i\zeta)}. \tag{S15}$$

The PDOS $\Sigma(\omega)$ projected onto the initial wave-packet $\psi_0(\mathbf{r})$ is given by

$$\Sigma(\omega) = \sum_{j=1}^{\infty} |c_j|^2 \delta(\omega - \epsilon_j), \tag{S16}$$

with $\delta(\omega - \epsilon_j)$ the Dirac delta. Then, applying the Sokhotski–Plemelj theorem to Equation S15, the PDOS $\Sigma(\omega)$ reads

$$\begin{aligned} \Sigma(\omega) &= \frac{1}{\pi} \lim_{\zeta \to 0^+} \mathrm{Re}\{ \langle \psi_0(\mathbf{r}) | \hat{\mathcal{L}}_\omega \psi(\mathbf{r},t) \rangle \}, \\ &= \frac{1}{\pi} \lim_{\zeta \to 0^+} \mathrm{Re}\{ \hat{\mathcal{L}}_\omega \underbrace{\langle \psi_0(\mathbf{r}) | \psi(\mathbf{r},t) \rangle}_{\mathrm{A}(t)} \}, \end{aligned} \tag{S17}$$

where $\mathrm{A}(t) = \langle \psi_0(\mathbf{r}) | \psi(\mathbf{r},t) \rangle$ is the autocorrelation function. Notice that the c_j in Equation S17 are the coefficients of $\psi_0(\mathbf{r})$ decomposed into the eigenfunctions of $\hat{H}$ (Equation S14), so that choosing different initial wave-packets $\psi_0(\mathbf{r})$ leads to a different PDOS $\Sigma(\omega)$.[16] This can be useful to focus on specific states with a special symmetry or spatial distribution, since only those states of the coupled QE–MNPs system that are not orthogonal to $\psi_0(\mathbf{r})$ can be accessed by the Wave-Packet Propagation method used to calculate the PDOS.

In practice, to address the PDOS for the $m = 0$ and $m = \pm 1$ symmetries, we choose a Gaussian-like initial wave-packet centered along the dimer z-axis at $\mathbf{r}_0 = \frac{1}{2} R_{\mathrm{qe}}\, \hat{\mathbf{z}}$ from the center of the QE (i.e., localized near the QE),

$$\psi_0(\mathbf{r}) = C |\mathbf{r} - \mathbf{r}_0|^{|m|}\, e^{i|m|\varphi}\, e^{-|\mathbf{r}-\mathbf{r}_0|^2/4}, \tag{S18}$$

where φ is the azimuth, m is the magnetic quantum number, and C is a normalization constant. We then propagate this $\psi_0(\mathbf{r})$ up to $T_f = 4000$ au according to Equation S11 and calculate the autocorrelation function $\mathrm{A}(t) = \langle \psi_0(\mathbf{r}) | \psi(\mathbf{r},t) \rangle$. Finally, using a small value

$\zeta = 0.1$ eV, we obtain the PDOS $\Sigma(\omega)$ corresponding to a subspace m from

$$\Sigma(\omega) = \frac{1}{\pi}\mathrm{Re}\{\int_0^{T_f} dt\, e^{i(\omega+i\zeta)t}\, A(t)\}. \tag{S19}$$

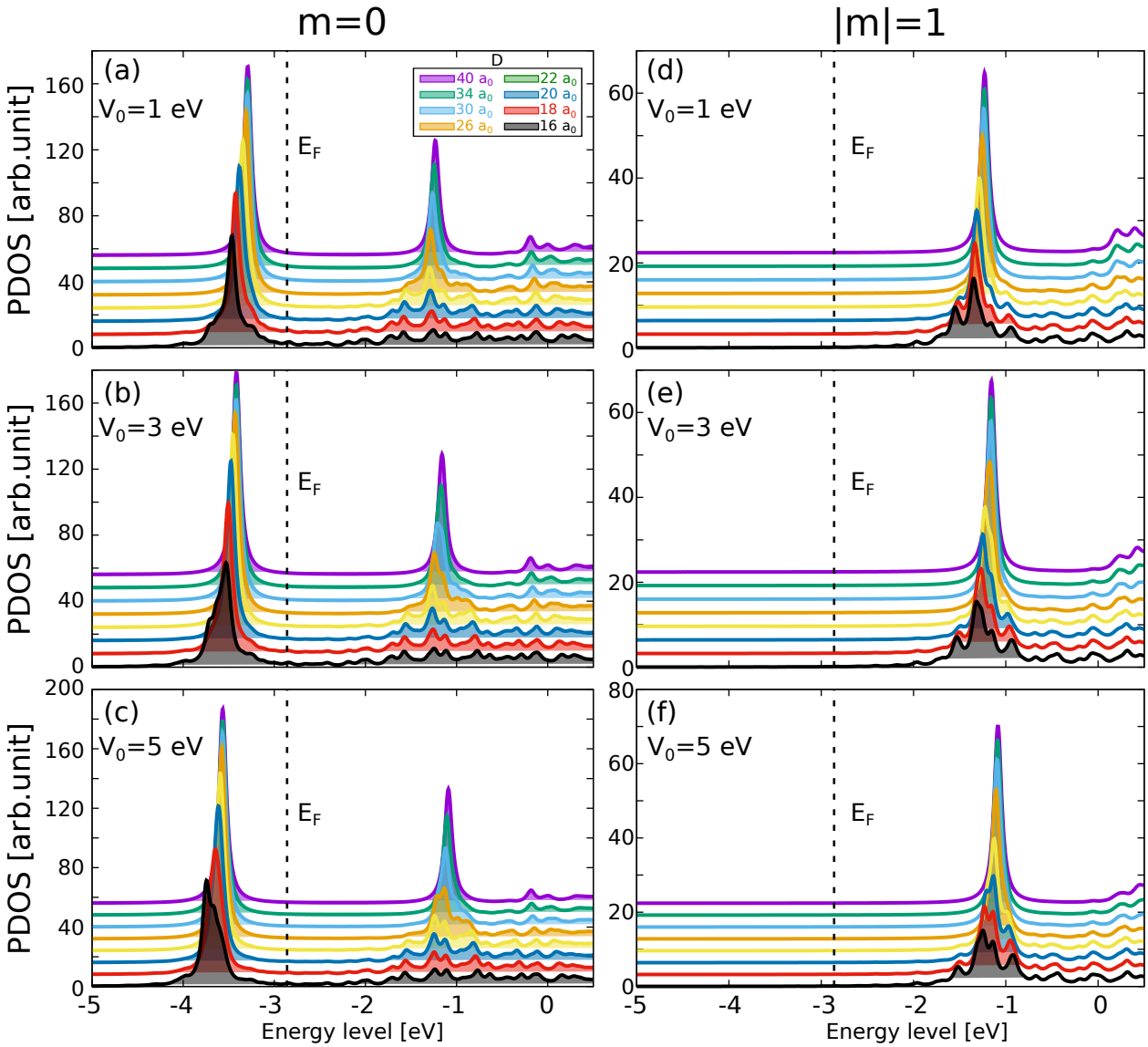

Figure S2: Projected density of electronic states localized at the QE in the middle of the gap. Results are shown as a function of the electron energy for different values of the gap size D ranging from $D = 16$ a$_0$ to $D = 40$ a$_0$ as displayed in the inset of panel **(a)**. The Fermi level $E_F = -2.86$ eV of the MNPs is depicted by a vertical dashed line. The panels of the figure correspond to the results obtained with different values of the background potential: **(a),(d)** $V_0 = 1$ eV, **(b),(e)** $V_0 = 3$ eV, and **(c),(f)** $V_0 = 5$ eV, and for different symmetry subspaces defined by the magnetic quantum number, m. Left-side panels **(a)-(c)**: $m = 0$, and right-side panels **(d)-(f)**: $|m| = 1$. Panel **(a)** corresponds to Figure 3 of the main text.

Figure S2 shows the evolution of the PDOS localized at the QE obtained for different

gap separation D ranging from $D = 16$ a_0 to $D = 40$ a_0 (see labels in panel a). Results are shown for two different magnetic quantum numbers $m = 0$ (left-side panels) and $|m| = 1$ (right-side panels), and for three different background QE potentials, $V_0 = 1$ eV, 3 eV and 5 eV. Note that the states with magnetic quantum number m and with $-m$ are degenerate due to the symmetry of the system. The radius of the QE is set to $R_{qe} = 5$ a_0, as in the main text and Figure S1.

Prior to the discussion of the PDOS, we recall that the KS energy structure of the ground-state QE is given by the $1s(\ell = 0,\ m = 0)$-orbital (doubly occupied and denoted as HOMO in the main text), while the triply-degenerate excited state is given by the $2p(\ell = 1,\ m = 0)$ and $2p(\ell = 1,\ m = \pm 1)$ orbitals. For z-polarized light, only the $2p(\ell = 1,\ m = 0)$ orbital is available for optical transitions from $1s$ and, for the sake of simplicity, it is called LUMO in the main text (see Subsection S1.1 for further details). As discussed below, the PDOS resolved by the m-symmetry subspace then reflects this electronic structure of the QE and shows similar qualitative behavior for the three values of V_0 considered.

For the $m = 0$ subspace, the evolution of the results with decreasing D is discussed in the main text. In brief, the PDOS obtained at large separation distances shows two well-defined peaks that corresponds to the E_{humo} and E_{lumo} energy levels of the isolated QE reported in Table S1. With decreasing D, the energies of the $1s$ (HOMO) and $2p$ (LUMO) orbitals slightly shift to lower values because of the attractive potential created by the MNPs. The peak corresponding to the $2p(\ell = 1,\ m = 0)$ (LUMO) state gradually vanishes owing to the increasing electronic coupling with the electronic states of the MNPs. The peak corresponding to the $1s(\ell = 0,\ m = 0)$ (HOMO) state also broadens, but to a lesser extent because the tighter-bound and thus better spatially-localized $1s$ orbital of the QE experiences less interaction with the MNPs.

In the $|m| = 1$ symmetry subspace, only one peak (near -1 eV) emerges at negative energies. According to the electronic structure of the QE, it corresponds to the excited $2p(\ell = 1,\ m = \pm 1)$ orbital. Notice that the ± 1 states are degenerate. The QE orbitals

of the $|m| = 1$ symmetry (one can also term these as $2p_x$ and $2p_y$ orbitals) are oriented perpendicular to the dimer z-axis. Their hybridization with $|m| = 1$ symmetry states of the MNPs is essentially smaller than that for the $2p_z$ (equivalently $2p(\ell = 1,\ m = 0)$) orbital of $m = 0$ symmetry. As a consequence, in this case, the resonant structure in the PDOS associated with the QE in Figure S2d,e,f stays well resolved up to the smallest D, in sheer contrast with the p-orbital of $m = 0$ symmetry (see higher-energy resonance near -1 eV in Figure S2a,b,c).

S3 Classical Optical Response of a QE–MNPs System

In this section, we explain the method used to obtain the classical optical response of the metallic dimer shown in Figure 1d and that of the coupled QE–MNPs system shown in Figures 2a and 5a of the main text. The numerical implementation used to obtain the optical response of the metallic dimer is based on the method reported in refs. 17 and 18, where the electromagnetic interaction is described within the nonretarded limit, justified because of the small size of the studied system.

S3.1 Optical response of a spherical dimer

We first consider the generic case of a dimer consisting of two spherical MNPs of radius R_1 and R_2 separated by a gap of size D. Each nanoparticle is characterized by a dielectric function $\varepsilon_1(\omega)$ and $\varepsilon_2(\omega)$, and the entire system is surrounded by a dielectric material of dielectric function $\varepsilon_d(\omega)$.

The nonretarded optical response of the system to an arbitrary external potential $\phi^{\text{ext}}(\mathbf{r}, \omega)$ oscillating at angular frequency ω is determined by the electrostatic potential $\phi^{\text{ind}}(\mathbf{r}, \omega) = \phi_1^{\text{ind}}(\mathbf{r}_1, \omega) + \phi_2^{\text{ind}}(\mathbf{r}_2, \omega)$ induced by the nanostructure, with $\phi_1^{\text{ind}}(\mathbf{r}_1, \omega)$ and $\phi_2^{\text{ind}}(\mathbf{r}_2, \omega)$ the potential induced by the nanoparticle 1 and 2, respectively. The vectors $\mathbf{r}_1 \equiv (r_1 \sin\theta_1 \cos\varphi_1, r_1 \sin\theta_1 \sin\varphi_1, r_1 \cos\theta_1)$ and $\mathbf{r}_2 \equiv (r_2 \sin\theta_2 \cos\varphi_2, r_2 \sin\theta_2 \sin\varphi_2, r_2 \cos\theta_2)$

are written in spherical coordinates with the origins at the center of the corresponding nanoparticle. We define the coordinates such that the centers of the MNPs are located at the z-axis separated by a distance $\delta = R_1 + D + R_2$, so that $\mathbf{r}_1$ and $\mathbf{r}_2$ are related by

$$\begin{aligned} r_2 &= \sqrt{r_1^2 + \delta^2 - 2\delta r_1 \cos\theta_1}, \\ \cos\theta_2 &= (r_1 \cos\theta_1 - \delta)/r_2, \\ \varphi_2 &= \varphi_1. \end{aligned} \tag{S20}$$

The induced electric potential $\phi^{\text{ind}}(\mathbf{r}, \omega)$ satisfies Laplace's equation

$$\nabla^2 \phi^{\text{ind}}(\mathbf{r}, \omega) = \nabla^2 \underbrace{\left(\phi_1^{\text{ind}}(\mathbf{r}_1, \omega) + \phi_2^{\text{ind}}(\mathbf{r}_2, \omega) \right)}_{\sum_{i=1}^{2} \phi_i^{\text{ind}}(\mathbf{r}_i, \omega)} = 0. \tag{S21}$$

(in Equation S21 and in the rest of this section we use subindexes i to refer to nanoparticle i, with $i = 1, 2$).

Due to the spherical symmetry of the nanoparticles, it is convenient to expand $\phi_i^{\text{ind}}(\mathbf{r}_i, \omega)$ inside ($r_i < R_i$) and outside ($r_i > R_i$) the metals in a spherical harmonics $Y_\ell^m(\theta_i, \varphi_i)$ basis set,

$$\begin{aligned} \phi_1^{\text{ind}}(\mathbf{r}_1, \omega) &= \sum_{\ell=1}^{\ell_{\max}} \sum_{m=-\ell}^{\ell} b_1^{\ell m}(\omega)\, Y_\ell^m(\theta_1, \varphi_1) \begin{cases} r_1^\ell / R_1^\ell & r_1 < R_1 \\ R_1^{\ell+1} / r_1^{\ell+1} & r_1 > R_1, \end{cases}, \\ \phi_2^{\text{ind}}(\mathbf{r}_2, \omega) &= \sum_{\ell=1}^{\ell_{\max}} \sum_{m=-\ell}^{\ell} b_2^{\ell m}(\omega)\, Y_\ell^m(\theta_2, \varphi_2) \begin{cases} r_2^\ell / R_2^\ell & r_2 < R_2 \\ R_2^{\ell+1} / r_2^{\ell+1} & r_2 > R_2, \end{cases}, \end{aligned} \tag{S22}$$

where $\ell_{\max}$ is an integer number large enough to achieve convergence.

The coefficients $b_i^{\ell m}(\omega)$ are obtained by applying the standard boundary conditions at the interfaces $r_i = R_i$,

$$\begin{aligned} \hat{\mathbf{n}}_i \times (\mathbf{E}_> - \mathbf{E}_<) &= 0, \\ \hat{\mathbf{n}}_i \cdot (\mathbf{D}_> - \mathbf{D}_<) &= 0, \end{aligned} \tag{S23}$$

where $\hat{\mathbf{n}}_i$ is the normal vector pointing from inside the metal ($<$) to outside ($>$), $\mathbf{E}(\mathbf{r},\omega)$ is the total electric field,

$$\mathbf{E}(\mathbf{r},\omega) = -\nabla\phi(\mathbf{r},\omega) = -\nabla\left(\phi^{\text{ext}}(\mathbf{r},\omega) + \phi^{\text{ind}}(\mathbf{r},\omega)\right), \tag{S24}$$

and $\mathbf{D}(\mathbf{r},\omega)$ is the electric displacement field in a medium with dielectric function $\varepsilon(\mathbf{r},\omega)$,

$$\mathbf{D}(\mathbf{r},\omega) = \varepsilon(\mathbf{r},\omega)\mathbf{E}(\mathbf{r},\omega). \tag{S25}$$

Applying the boundary conditions given by Equation S23 results in the following expressions for the coefficients $b_i^{\ell m}(\omega)$

$$\begin{aligned} b_1^{\ell m}(\omega) &= \frac{-R_1(\varepsilon_1-\varepsilon_d)}{\varepsilon_d(\ell+1)+\varepsilon_1\ell}\int_{\Omega_1} d\Omega_1\,[Y_\ell^m(\theta_1,\varphi_1)]^*\frac{\partial}{\partial r_1}\left(\phi^{\text{ext}}(\mathbf{r}_1,\omega)+\phi_2^{\text{ind}}(\mathbf{r}_2,\omega)\right)|_{r_1=R_1}, \\ b_2^{\ell m}(\omega) &= \frac{-R_2(\varepsilon_2-\varepsilon_d)}{\varepsilon_d(\ell+1)+\varepsilon_2\ell}\int_{\Omega_2} d\Omega_2\,[Y_\ell^m(\theta_2,\varphi_2)]^*\frac{\partial}{\partial r_2}\left(\phi^{\text{ext}}(\mathbf{r}_2,\omega)+\phi_1^{\text{ind}}(\mathbf{r}_1,\omega)\right)|_{r_2=R_2}, \end{aligned} \tag{S26}$$

with the integrals extending over the solid angles $\Omega_i = \{\theta_i, \phi_i\}$.

From Equation S22, the coefficients $b_1^{\ell m}(\omega)$ and $b_2^{\ell m}(\omega)$ in Equation S26 can be written in matrix form,

$$\begin{aligned} b_1^{\ell m}(\omega) &= \left(\mathbb{I}-\mathbb{T}^{2\to1}\mathbb{T}^{1\to2}\right)^{-1}\left(b_1^{\ell m,\text{ext}}(\omega)+\mathbb{T}^{2\to1}b_2^{\ell m,\text{ext}}(\omega)\right), \\ b_2^{\ell m}(\omega) &= \left(\mathbb{I}-\mathbb{T}^{1\to2}\mathbb{T}^{2\to1}\right)^{-1}\left(b_2^{\ell m,\text{ext}}(\omega)+\mathbb{T}^{1\to2}b_1^{\ell m,\text{ext}}(\omega)\right), \end{aligned} \tag{S27}$$

where $\mathbb{I}$ is the identity matrix,

$$\begin{aligned} b_1^{\ell m,\text{ext}}(\omega) &= \frac{-R_1(\varepsilon_1-\varepsilon_d)}{\varepsilon_d(\ell+1)+\varepsilon_1\ell}\int_{\Omega_1} d\Omega_1\,[Y_\ell^m(\theta_1,\varphi_1)]^*\frac{\partial}{\partial r_1}\phi^{\text{ext}}(\mathbf{r}_1,\omega)|_{r_1=R_1}, \\ b_2^{\ell m,\text{ext}}(\omega) &= \frac{-R_2(\varepsilon_2-\varepsilon_d)}{\varepsilon_d(\ell+1)+\varepsilon_2\ell}\int_{\Omega_2} d\Omega_2\,[Y_\ell^m(\theta_2,\varphi_2)]^*\frac{\partial}{\partial r_2}\phi^{\text{ext}}(\mathbf{r}_2,\omega)|_{r_2=R_2}, \end{aligned} \tag{S28}$$

and the elements $(\ell m, \ell' m')$ of matrices $\mathbb{T}^{2\to1}$ and $\mathbb{T}^{1\to2}$ are given by

$$\begin{aligned}
\mathbb{T}^{2\to1}_{\ell m,\ell' m'} &= \frac{-R_1(\varepsilon_1-\varepsilon_d)}{\varepsilon_d(\ell+1)+\varepsilon_1\ell}\int_{\Omega_1} d\Omega_1[Y^m_\ell(\theta_1,\varphi_1)]^*\frac{\partial}{\partial r_1}\left(Y_{\ell' m'}(\theta_2,\varphi_2)\frac{R_2^{\ell'+1}}{r_2^{\ell'+1}}\right)|_{r_1=R_1},\\
\mathbb{T}^{1\to2}_{\ell m,\ell' m'} &= \frac{-R_2(\varepsilon_2-\varepsilon_d)}{\varepsilon_d(\ell+1)+\varepsilon_2\ell}\int_{\Omega_2} d\Omega_2[Y^m_\ell(\theta_2,\varphi_2)]^*\frac{\partial}{\partial r_2}\left(Y_{\ell' m'}(\theta_1,\varphi_1)\frac{R_1^{\ell'+1}}{r_1^{\ell'+1}}\right)|_{r_2=R_2}.
\end{aligned} \tag{S29}$$

Once the coefficients $b_1^{\ell m}(\omega)$ and $b_2^{\ell m}(\omega)$ are obtained by solving Equation S27, the electric potential induced by each metallic nanoparticle is completely determined according to Equation S22.

Moreover, we can calculate other physical quantities of interest using the same coefficients $b_i^{\ell m}(\omega)$. For example, the electric field induced by the metallic dimer at position $\mathbf{r}$ is directly related to the induced potential (Equation S24) and is given by the sum of the field induced by each metallic nanoparticle i,

$$\mathbf{E}^{\text{ind}}(\mathbf{r},\omega) = -\sum_{i=1}^{2}\nabla\phi_i^{\text{ind}}(\mathbf{r}_i,\omega) = -\sum_{i=1}^{2}\sum_{\ell=1}^{\ell_{\max}}\sum_{m=-\ell}^{\ell} b_i^{\ell m}(\omega)\,\nabla\left(Y^m_\ell(\theta_i,\varphi_i)R_i^{\ell+1}/r_i^{\ell+1}\right). \tag{S30}$$

In a similar way, the total induced dipole moment is also given by the sum of two contributions,

$$\mathbf{p}_{\text{dimer}}(\omega) = \sum_{i=1}^{2}\sum_{m=-1}^{m=1} b_i^{1m}(\omega)Y_1^m(\theta_i,\varphi_i)\,R_i^2\,\hat{\mathbf{r}}_i, \tag{S31}$$

where $\hat{\mathbf{r}}_i = \mathbf{r}_i/r_i$ is the unit vector with its origin at the center of the nanoparticle i.

In all the classical results shown in the main text and in this Supporting Information for the Na dimer, we consider two identical nanoparticles of radius $R_1 = R_2 = R_{MNP} = 34.4\,\text{a}_0$ surrounded by vacuum ($\varepsilon_d = 1$). The dielectric function of the MNPs is described within the Drude model,

$$\varepsilon_1(\omega) = \varepsilon_2(\omega) = \varepsilon(\omega) = 1 - \frac{\omega_p^2}{\omega^2 + i\gamma_p\omega}, \tag{S32}$$

where the values of the plasma frequency $\omega_p = 5.43$ eV and the intrinsic damping $\gamma_p = 0.15$ eV are obtained by adjusting the classical optical response of an individual MNP to

that calculated with TDDFT. Details are given in Subsection S3.3.

In all the classical calculations we also introduce a gap scaling[19–21] of $\Delta = 3.4\ \mathrm{a_0}$ to (partially) account for the spill-out of the induced density with respect to the geometrical surface of the nanoparticles (correctly captured by the TDDFT simulations). Thus, in Figures 1d, 2a-b, and 5a-b of the main text, the TDDFT results obtained for a gap separation D_{TDDFT} are compared to the corresponding classical results with an effective gap separation $D_{\mathrm{classical}} = D_{\mathrm{TDDFT}} - \Delta$. D_{TDDFT} is defined as the minimum distance between the jellium edges of the two spherical nanoparticles. For simplicity, we use the symbol D to refer to both $D_{\mathrm{classical}}$ and D_{TDDFT}. This distance scaling Δ is also included in all the classical results shown in the this Supporting Information.

The classical absorption cross-section spectra of the isolated metallic dimer, $\sigma_{\mathrm{dimer}}(\omega) = \frac{4\pi\omega}{c}\mathrm{Im}\{\alpha_{\mathrm{dimer}}(\omega)\}$, shown in Figure 1d of the main text, are obtained by using in Equation S26 the following external potential

$$\phi^{\mathrm{ext}}(\mathbf{r},\omega) = \phi^{\mathrm{ext}}(\mathbf{r}_1,\omega) = -\mathrm{E}_0 r_1 \cos\theta_1, \tag{S33}$$

associated with a spatially-constant electric field of amplitude E_0 oriented along the z-axis (corresponding to a z-polarized plane wave within the nonretarded limit). For this illumination, the induced dipole moment is polarized along the z-axis, $\mathbf{p}_{\mathrm{dimer}}(\omega) = \hat{\mathbf{z}}\, p_{\mathrm{dimer}}(\omega)$, and the polarizability $\alpha_{\mathrm{dimer}}(\omega)$ of the isolated dimer reads

$$\alpha_{\mathrm{dimer}}(\omega) = p_{\mathrm{dimer}}(\omega)/\mathrm{E}_0. \tag{S34}$$

In Figure S3a, we show the classical nonretarded absorption spectra of the isolated Na dimer obtained for different values of the gap separation D. The separation distance ranges from $D = 16\ \mathrm{a_0}$ to $D = 40\ \mathrm{a_0}$, as in Figures 2a-b and 5a-b of the main text. In Figure S3b we display the corresponding TDDFT results, and overall good agreement between the two calculations is observed in the strength and the spectral position of the dominant

bonding dipolar plasmon resonance (BDP, green dots). However, for small interparticle distance D, the BDP resonance becomes broader and weaker within the TDDFT framework as compared to the classical results. For the range of interparticle distance considered in this work, electron tunneling in vacuum junctions is negligible, and thus we ascribe the differences in the BDP resonance between the two models to nonlocal dynamical screening and finite-size effects[22] present in small metallic nanoparticles (only accounted for by the TDDFT calculations). As discussed in the main text, the bonding quadrupolar plasmon (BQP, red dots) resonance is not developed in the TDDFT results because of the small size of the MNPs considered here.

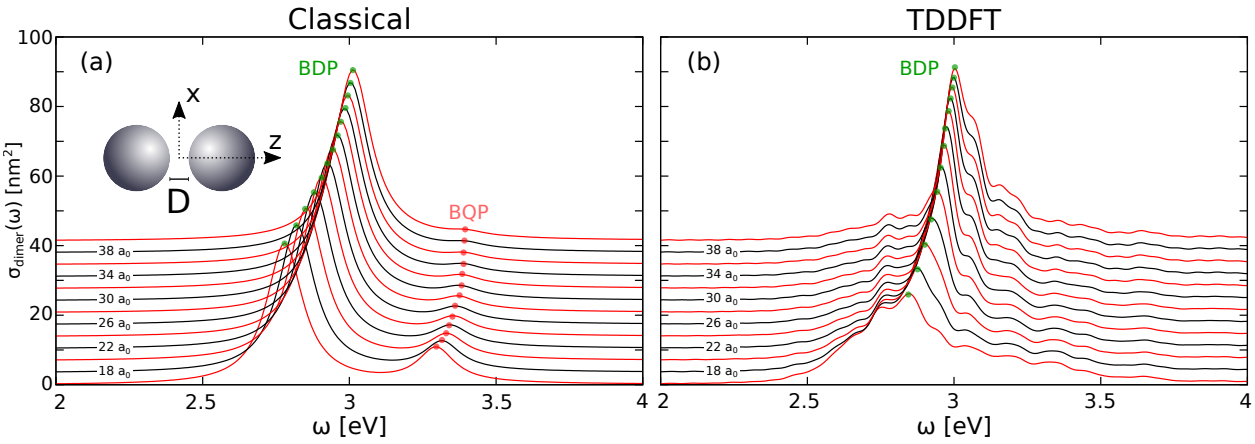

Figure S3: Waterfall plots of the absorption cross-section of the isolated Na metallic dimer of radius $R_{\mathrm{MNP}} = 34.4\ \mathrm{a_0}$. The incident electromagnetic plane wave is polarized along the dimer axis (z-axis). Results of the **(a)** classical and **(b)** TDDFT calculations are shown as function of the gap size D ranging from $D = 16\ \mathrm{a_0}$ (lower spectra) to $D = 40\ \mathrm{a_0}$ (upper spectra). The D value is indicated at each second spectrum marked by the black lines. The bonding dipolar (BDP) and quadrupolar (BQP) plasmon resonances are marked with green and red dots, respectively.

S3.2 Electromagnetic QE–MNPs interaction

In this subsection, we explain how to obtain the classical optical response of the coupled QE–MNPs system shown in Figures 2a and 5a of the main text. Adopting the Green's function formalism,[8,23] we decompose the induced dipole of the total QE–MNPs structure, $\mathbf{p}(\omega) = \mathbf{p}_{\mathrm{dimer}}(\omega) + \mathbf{p}_{\mathrm{qe}}(\omega)$, as a sum of the MNPs dipole, $\mathbf{p}_{\mathrm{dimer}}(\omega)$, and that of the QE, $\mathbf{p}_{\mathrm{qe}}(\omega)$. The QE, located at position $\mathbf{r} = \mathbf{r}_{\mathrm{QE}}$, is described as a point dipole.

The electromagnetic QE–MNPs interaction can be understood as follows: the MNPs induce an electric near field $\mathbf{E}^{\text{ind}}(\mathbf{r},\omega)$ in response to an external (spatially-constant) illumination $\mathbf{E}_0$. Then, $\mathbf{E}^{\text{ind}}(\mathbf{r},\omega)$ and $\mathbf{E}_0$ induce a dipole moment at the QE, $\mathbf{p}_{\text{qe}}(\omega)$, which acts back on itself due to the presence of the MNPs *via* the self-interaction Green's tensor, $\hat{\mathbb{G}}(\mathbf{r}_{\text{QE}},\mathbf{r}_{\text{QE}},\omega)$. Finally, the dipole moment created at the QE, $\mathbf{p}_{\text{qe}}(\omega)$, induces a dipole moment at the MNPs due to the electromagnetic interaction. This physical picture can be described with the following equations for $\mathbf{p}_{\text{qe}}(\omega)$ and $\mathbf{p}_{\text{dimer}}(\omega)$,[24]

$$\begin{aligned}
\mathbf{p}_{\text{qe}}(\omega) &= \alpha_{\text{qe}}(\omega)\left(\mathbb{I}-\alpha_{\text{qe}}(\omega)\hat{\mathbb{G}}(\mathbf{r}_{\text{QE}},\mathbf{r}_{\text{QE}},\omega)\right)^{-1}\left(\mathbf{E}_0+\mathbf{E}^{\text{ind}}(\mathbf{r}=\mathbf{r}_{\text{QE}},\omega)\right),\\
\mathbf{p}_{\text{dimer}}(\omega) &= \hat{\alpha}_{\text{dimer}}(\omega)\mathbf{E}_0+\hat{\alpha}^{\text{QE}}_{\text{dimer}}(\omega)\mathbf{p}_{\text{qe}}(\omega),
\end{aligned} \tag{S35}$$

where

- $\mathbb{I}$ is the identity matrix.
- $\alpha_{\text{qe}}(\omega)$ is the classical polarizability of the point-dipole QE obtained from Equation S8. See Table S1 for the parameters used to describe the QE.
- $\mathbf{E}^{\text{ind}}(\mathbf{r}=\mathbf{r}_{\text{QE}},\omega)$ is the electric field induced by the metallic nanoparticle at the position of the QE, $\mathbf{r}_{\text{QE}}$, in response to the external illumination $\mathbf{E}_0$. In this work, $\mathbf{r}_{\text{QE}}$ corresponds to the center of the gap at the dimer z-axis, and since the external illumination is polarized along the z-axis, $\mathbf{E}_0=\hat{\mathbf{z}}\,\text{E}_0$, $\mathbf{E}^{\text{ind}}(\mathbf{r}=\mathbf{r}_{\text{QE}},\omega)$ is also z-polarized. $\mathbf{E}^{\text{ind}}(\mathbf{r}=\mathbf{r}_{\text{QE}},\omega)$ is obtained from Equation S30 using the external potential of Equation S33.
- $\hat{\alpha}_{\text{dimer}}(\omega)$ is the polarizability tensor of the metallic dimer. Due to the geometry considered here, this polarizability can be treated as a scalar, $\alpha_{\text{dimer}}(\omega)$, and it can be obtained from Equation S34 using the external potential of Equation S33.
- $\hat{\mathbb{G}}(\mathbf{r}_{\text{QE}},\mathbf{r}_{\text{QE}},\omega)$ is the self-interaction Green's tensor that gives the electric field induced by the metallic nanoparticles at $\mathbf{r}_{\text{QE}}$ in response to a unitary point-dipole

QE located at the same position $\mathbf{r}_{\mathrm{QE}}$. Due to the geometry considered in this work, $\hat{\mathbb{G}}(\mathbf{r}_{\mathrm{QE}}, \mathbf{r}_{\mathrm{QE}}, \omega)$ also becomes scalar, $\mathbb{G}(\mathbf{r}_{\mathrm{QE}}, \mathbf{r}_{\mathrm{QE}}, \omega)$. We obtain $\mathbb{G}(\mathbf{r}_{\mathrm{QE}}, \mathbf{r}_{\mathrm{QE}}, \omega)$ using the methodology explained in the previous subsection but considering the external potential created by a z-polarized classical dipole of amplitude P_0,

$$\phi^{\mathrm{ext}}(\mathbf{r}, \omega) = \phi^{\mathrm{ext}}(\mathbf{r}_1, \omega) = \mathrm{P}_0 \, \hat{\mathbf{z}}_1 \cdot \frac{\mathbf{r}_1 - \mathbf{r}_{\mathrm{QE}}}{|\mathbf{r}_1 - \mathbf{r}_{\mathrm{QE}}|^3}, \tag{S36}$$

so that, according to Equations S22 and S30,

$$\mathbb{G}(\mathbf{r}_{\mathrm{QE}}, \mathbf{r}_{\mathrm{QE}}, \omega) = -\frac{1}{\mathrm{P}_0} \nabla \left(\phi_1^{\mathrm{ind}}(\mathbf{r}_1 = \mathbf{r}_{\mathrm{QE}}, \omega) + \phi_2^{\mathrm{ind}}(\mathbf{r}_2 = \mathbf{r}_{\mathrm{QE}}, \omega) \right). \tag{S37}$$

The real (panel a) and imaginary (panel b) parts of the self-interaction Green's function $\mathbb{G}(\mathbf{r}_{\mathrm{QE}}, \mathbf{r}_{\mathrm{QE}}, \omega)$ obtained for the Na dimer with different gap separations D are shown in Figure S4. With decreasing D, $\mathbb{G}(\mathbf{r}_{\mathrm{QE}}, \mathbf{r}_{\mathrm{QE}}, \omega)$ is generally larger in magnitude, and the relative contribution of the high-order plasmonic modes at $\omega \sim 3.3 - 3.8$ eV becomes more important.

- $\hat{\alpha}_{\mathrm{dimer}}^{\mathrm{QE}}(\omega)$ is a tensor that provides the dipole moment induced at the metallic dimer in response to the electromagnetic field created by a classical point dipole located at $\mathbf{r}_{\mathrm{QE}}$. Due to the geometry of our system, it can be treated as a scalar, $\alpha_{\mathrm{dimer}}^{\mathrm{QE}}(\omega)$. We obtain $\alpha_{\mathrm{dimer}}^{\mathrm{QE}}(\omega)$ from the induced dipole moment (normalized to P_0) according to Equation S31, using the external potential of Equation S36.

In summary, the optical response of the studied QE–MNPs system is obtained in three steps: first, we calculate $\mathbf{E}^{\mathrm{ind}}(\mathbf{r} = \mathbf{r}_{\mathrm{QE}}, \omega)$ and $\alpha_{\mathrm{dimer}}(\omega)$ by solving Equations S27 for the external potential of Equation S33. Second, $\mathbb{G}(\mathbf{r}_{\mathrm{QE}}, \mathbf{r}_{\mathrm{QE}}, \omega)$ and $\alpha_{\mathrm{dimer}}^{\mathrm{QE}}(\omega)$ are obtained by solving the same equations but considering the external potential given by Equation S36. Finally, we use Equation S35 to calculate the total dipole moment induced at the coupled system, $\mathbf{p}(\omega) = \mathbf{p}_{\mathrm{dimer}}(\omega) + \mathbf{p}_{\mathrm{qe}}(\omega)$, which, due to the geometry of the considered

configuration, is oriented along the z direction, $\mathbf{p}(\omega) = \hat{\mathbf{z}}\, p(\omega)$. We can then obtain the classical absorption cross-section using the relation $\sigma(\omega) = \frac{4\pi\omega}{c}\mathrm{Im}\{\alpha(\omega)\}$, where $\alpha(\omega) = p(\omega)/\mathrm{E}_0$ is the polarizability of the coupled QE–MNPs system.

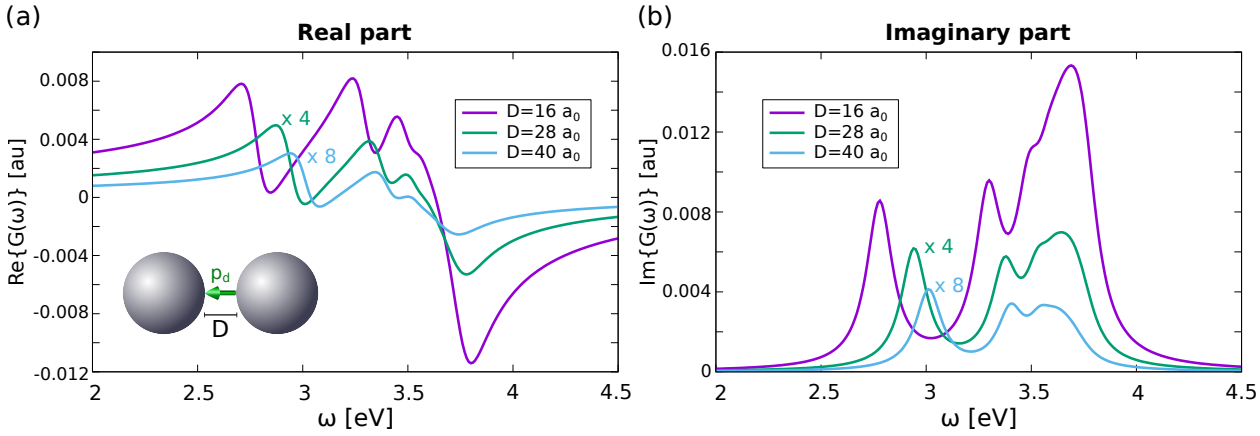

Figure S4: **(a)** Real and **(b)** imaginary part of the self-interaction Green's function, $\mathbb{G}(\mathbf{r}_{\mathrm{QE}}, \mathbf{r}_{\mathrm{QE}}, \omega)$, calculated for a point dipole aligned along the dimer z-axis and placed at $\mathbf{r}_{\mathrm{QE}}$ in the center of the gap between two identical Na nanoparticles of radius $R_{MNP} = 34.4$ a_0. Results are obtained from classical nonretarded calculations for different gap sizes $D = 16$ a_0, 28 a_0, and 40 a_0, as indicated in the insets. The local dielectric function of Na used in the calculations is given by the Drude model discussed in Section S3.3.

S3.3 Extracting parameters for the Drude dielectric function

In order to choose the values of the parameters ω_p and γ_p determining the local Drude dielectric function of the Na nanoparticle dimer, we fit the TDDFT absorption spectrum of an individual spherical nanoparticle of radius $R_{MNP} = 34.4$ a_0,

$$\sigma_{\mathrm{mnp}}(\omega) = \frac{4\pi\omega}{c}\mathrm{Im}\{\alpha_{\mathrm{mnp}}(\omega)\}, \tag{S38}$$

to the corresponding classical result obtained with the following polarizability

$$\alpha_{\mathrm{mnp}}(\omega) = \alpha_{\mathrm{mnp}}^{\mathrm{classical}}(\omega) = R_{MNP}^3 \frac{\varepsilon(\omega) - 1}{\varepsilon(\omega) + 2}, \tag{S39}$$

where the Drude dielectric function $\varepsilon(\omega)$ is given by Equation S32.

The TDDFT results are obtained for an individual Na nanoparticle characterized by

the same Wigner–Seitz radius ($r_s = 4$ a$_0$) and the same number of conduction electrons (N=638) as the nanoparticles considered in the main text.

As shown in Figure S5, $\omega_p = 5.43$ eV and $\gamma_p = 0.15$ eV provide reasonably good agreement between the classical and the TDDFT results. The "effective" plasma frequency ω_p is slightly smaller than the nominal bulk plasma frequency of the free-electron gas corresponding to the density parameter $r_s = 4$ a$_0$ used in the TDDFT simulations ($\omega_p = \sqrt{\frac{3}{r_s^3}} = 5.89$ eV). This small modification of the bulk plasma frequency allows us to account for the redshift of the dipolar plasmon frequency of the small metal nanoparticle because of the electron spill-out and dynamical screening.[25] On the other hand, γ_p accounts for all the decay channels of the plasmon excitation including the contribution of Landau damping.[26,27]

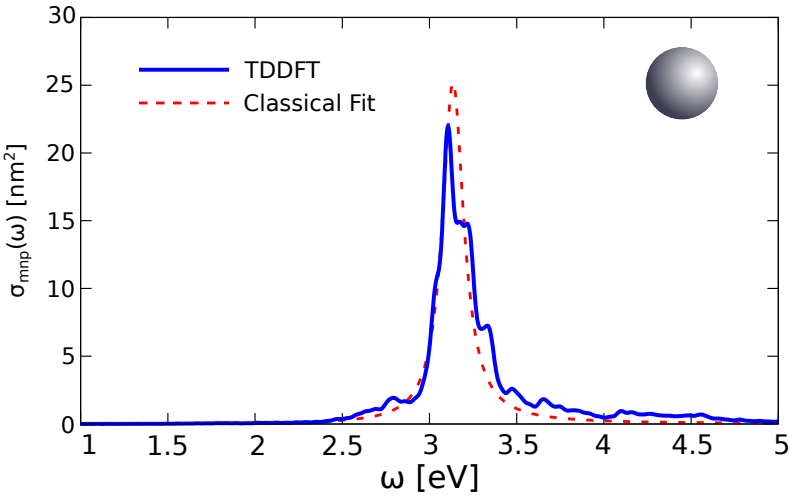

Figure S5: Absorption cross-section of an individual metallic nanoparticle of radius $R_{\mathrm{MNP}} = 34.4$ a$_0$ as obtained from TDDFT (solid blue line) and classical (dashed red line) calculations. For the TDDFT results, we use a Wigner–Seitz radius of $r_s = 4$ a$_0$. For the classical results, we use a Drude dielectric function with plasma frequency $\omega_p = 5.43$ eV and intrinsic damping $\gamma_p = 0.15$ eV.

S4 Role of the Electronic QE–MNPs Coupling in a Resonant Exciton–Plasmon Hybrid System

In the main text, we provide a detailed discussion of the impact of the electronic QE–MNPs coupling on the optical response in a situation where the exciton energy of the isolated QE is out of resonance with the BDP mode of the metallic dimer, as shown in Figure 2 of the main text. However, the general underlying physics owing to quantum effects holds irrespective of the detuning between the QE exciton and the BDP of the metallic dimer as we demonstrate in Figure 5 of the main text. Figure 5 corresponds to the situation where the QE exciton energy is resonant with the BDP mode of the dimer antenna. This choice is convenient to analyze the regime of strong electromagnetic coupling (or, in short, strong coupling) between the exciton and the plasmon, where the coupling overcomes the losses and hybrid polaritonic states are formed. We thus discuss the resonant situation in more detail in this section showing that indeed we reach the strong-coupling regime.

In Figure 5 of the main text, we compare the absorption spectra of the resonant QE–MNPs system as obtained from classical (panel a) and TDDFT (panel b) simulations. Results are shown as waterfall plots by varying the gap separation from $D = 40$ a_0 (top) to $D = 16$ a_0 (down). We calculate the TDDFT spectra in the same manner as for Figure 2b of the main text, with the only difference that in this section we use a background QE potential of $V_0 = 5$ eV (see Section S1). The classical results are obtained for a point-like QE characterized by an oscillator strength $\alpha_0 = 1.52$ au, a resonant energy $\omega_0 = 2.95$ eV, and a decay rate $\gamma_{qe} = 70$ meV (see Table S1), following the procedure explained in Section S3.

The classical model predicts a splitting between the lower (LR, blue dots) and the upper (UR, green dots) resonances with respect to the resonant energy ω_0 of the isolated QE already for large interparticle distance $D = 40$ a_0. This LR–UR splitting is a signature of the strong coupling between the QE exciton and the BDP resonance of the metallic dimer, as we further confirm in Subsection S4.1. With decreasing D, the LR–UR energy differ-

ence strongly increases within the classical model owing to the stronger electromagnetic hybridization between the exciton and the plasmon. Moreover, within the classical framework the higher-order plasmonic modes of the MNPs contribute to the electromagnetic interactions between the dimer and the QE for small gap separations. The effect of these higher-order modes, well documented for isolated dimer antennas,[28] results here in an additional redshift of both the LR and UR branches, which explains why the UR branch appears at lower energies than the exciton energy $\omega_0 = 2.95$ eV of the isolated QE. These aspects are discussed in more detail in Subsection S4.1.

The TDDFT results in Figure 5b of the main text also show a splitting between the LR and the UR with respect to ω_0 for large interparticle distance $D = 40$ a_0, although the strength of the LR is weaker than the one predicted by the classical model. This difference is a consequence of the nonlocality and finite-size effects that affect the optical response of the isolated metallic dimer, as confirmed by the results obtained with a *semiclassical* model that we show in Section S5 below. Indeed, there is no QE exciton quenching produced by electronic hybridization for large separation, since at those distances the electronic QE–MNPs coupling does not play a role. However, upon reducing the gap size D, the electronic orbitals of the QE hybridize with these of the MNPs. The LUMO evolves into a broad structure (see PDOS in Figure S2) reflecting the fast transfer of the excited electron between the LUMO of the QE and the conduction band states of the MNPs quantized by the finite-size effect. This electronic interaction has an immediate consequence on the optical response of the system. The LR–UR splitting is drastically reduced as compared to the classical predictions, and the LR and UR branches progressively merge into a broad spectral feature at small D.

These differences in the absorption spectra between the classical and TDDFT results are similar to the findings discussed in the main text for the off-resonant case (Figure 2), where we analyzed a blueshift and subsequent disappearance of the LR produced by the electronic QE–MNPs coupling for decreasing gap separation D below $D \sim 26$ a_0. With the

analysis of the resonant system, which is classically in the strong-coupling regime (see subsection S4.1), we show that the reduction of the lifetime of the QE exciton because of the electronic hybridization between the QE and the MNPs orbitals attenuates the LR–UR splitting of the absorption resonances. At small separations, the electronic QE–MNPs coupling finally results in the disappearance of the distinct feature of the LR from the absorption spectra. Therefore, this electronic effect linked with the excited-electron transport between the QE and the MNPs should be taken into account to correctly describe the optical response of the interacting QE–MNPs system both in resonant and off-resonant conditions. The key role of the electronic coupling is further confirmed by a *semiclassical* model presented in Section S5.

S4.1 Analysis of the coupling strength g to identify the strong-coupling regime

In this subsection, we analyze the coupling strength g as derived from the classical electromagnetic simulations for the resonant exciton–plasmon system shown in this section and in Figure 5 of the main text. Knowing the value of g (and of the other parameters of the system) allows for identifying whether the system is in the strong-coupling regime.

In order to obtain the coupling strength g between the exciton and the BDP mode of the dimer of MNPs, we fit the frequency-dependent absorption cross section $\sigma_{\text{abs}}(\omega)$ of the coupled QE–MNPs structure to the analytical expression derived from a classical coupled-oscillators model driven by the excitation of the BDP of the metallic nanoantenna,[29]

$$\sigma_{\text{abs}}(\omega) = A\,\omega \times \\ \text{Im}\left\{ \frac{(\omega_0 - \Delta\omega_0)^2 - (\omega + i\gamma_{\text{QE}}/2)^2}{\left(\omega_{\text{BDP}}^2 - (\omega + i\gamma_{\text{p}}/2)^2\right)\left((\omega_0 - \Delta\omega_0)^2 - (\omega + i\gamma_{\text{QE}}/2)^2\right) - 4g^2\omega^2} \right\}, \tag{S40}$$

where Im{ } stands for the imaginary part. In Equation S40, $\gamma_{\text{QE}} = 70$ meV and

$\gamma_p = 150$ meV are the damping rates of the isolated quantum emitter and bonding dimer plasmon respectively, $\omega_0 = 2.95$ eV is the QE exciton energy, and ω_{BDP} is the energy of the BDP resonance. As shown in Figure S3, ω_{BDP} depends on the gap size D, so that for each gap separation the corresponding value of ω_{BDP} obtained from classical calculations (see Section S3) is used. The free (fitting) parameters are

- the amplitude A,
- the coupling strength g between the QE exciton and the BDP resonance of the dimer antenna,
- the redshift $\Delta\omega_0$ of the QE exciton energy induced by the interaction with high-order plasmon modes.

$\Delta\omega_0$ corresponds to the redshift (analog of the Lamb shift) of the QE exciton induced by high-order plasmon modes and needs to be introduced because in the derivation of Equation S40, the system was projected onto the subspace of only 2 interacting excitations: the QE exciton and the BDP of the dimer.

This interaction of the QE exciton with high-order plasmonic resonances increases with decreasing D, and therefore the redshift $\Delta\omega_0$ is larger for smaller D. We obtain $\Delta\omega_0 = 0.02$ eV for $D = 40$ a_0, and $\Delta\omega_0 = 0.67$ eV for $D = 16$ a_0. The hybrid QE–MNPs system is then equivalent to a BDP of the dimer interacting with a QE exciton of an effective frequency $\omega_0 - \Delta\omega_0$. We note that the resonant frequency ω_{BDP} of the BDP also depends on the gap size D (Figure S3). As a consequence, it is not possible to choose the parameters of the QE such that the effective frequency $\omega_0 - \Delta\omega_0$ and the frequency of the BDP perfectly match irrespective of D. However, for the system considered in our study, the coupling strength g is systematically larger than the frequency detuning between the BDP and the effective exciton frequency $\omega_0 - \Delta\omega_0$ (see below). It is only for the small gap sizes $D = 16 - 20$ a_0 that the situation is reversed. Thus, the canonical criteria of the strong coupling can be applied.

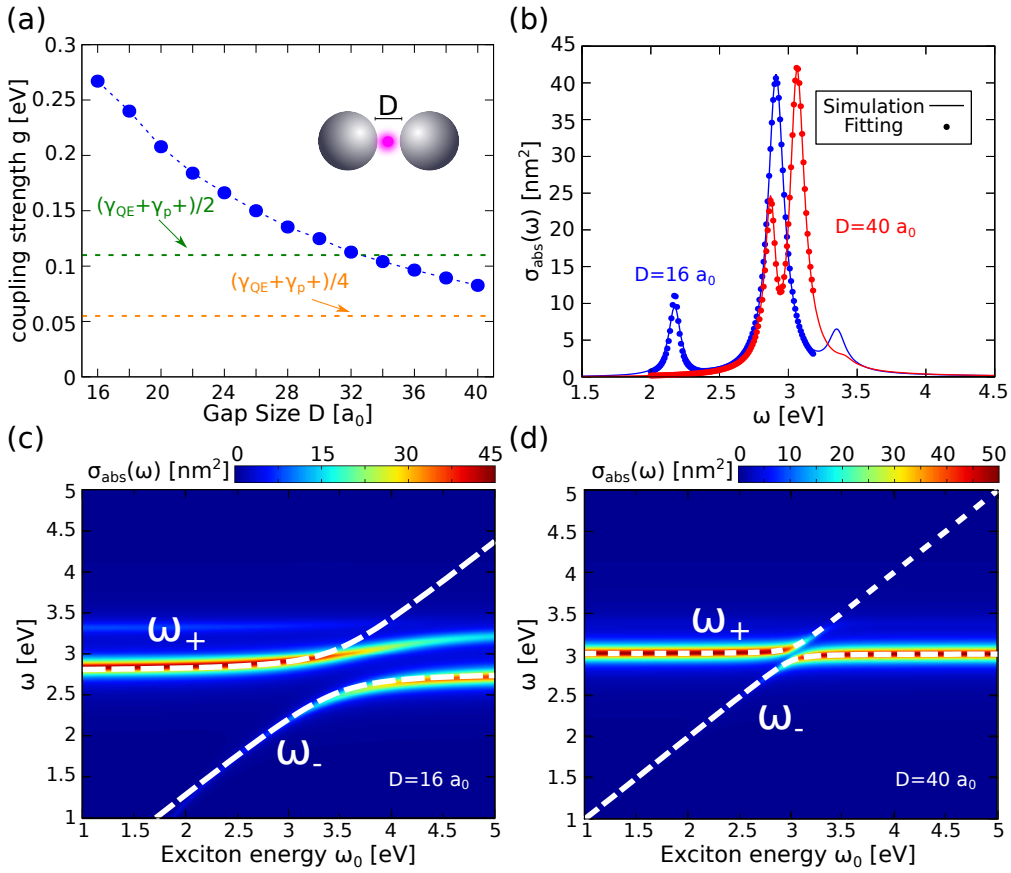

Figure S6: **(a)** Coupling strength g obtained for the resonant QE–MNPs system for different values of the gap size D. The values $(\gamma_{\mathrm{QE}} + \gamma_p)/4$ and $(\gamma_{\mathrm{QE}} + \gamma_p)/2$ are depicted by orange and green lines, respectively. **(b)** Solid lines: absorption cross section $\sigma_{\mathrm{abs}}(\omega)$ calculated using the classical electrodynamics framework. Dots: Fit of the classical results by the coupled oscillator model given by Equation S40. Results are shown as a function of the frequency ω of the incident electromagnetic plane wave polarized along the dimer axis. The coupled QE–MNPs system is characterized by a gap size $D = 16$ a$_0$ (blue line, blue dots) and $D = 40$ a$_0$ (red line, red dots). **(c)-(d)** Color maps of the absorption cross section $\sigma_{\mathrm{abs}}(\omega)$ obtained from classical electrodynamics simulations for the coupled QE–MNPs system for $D = 16$ a$_0$ (panel c) and $D = 40$ a$_0$ (panel d). The incident electromagnetic plane wave is polarized along the dimer axis. Results are shown as a function of the frequency ω of the incident electromagnetic plane wave, and of the energy of the QE exciton ω_0. Dashed white lines represent the upper (ω_+) and the lower (ω_-) polaritons obtained from Equation S41, using $\Delta\omega = 0.67$ eV ($D = 16$ a$_0$) and $\Delta\omega = 0.02$ eV ($D = 40$ a$_0$) for all the values of ω_0.

Figure S6a shows the coupling strength g obtained by fitting the classical absorption cross section $\sigma_{\mathrm{abs}}(\omega)$ of the resonant QE–MNPs system to Equation S40 for different values of the gap size D. The coupling strength g for the present system monotonically increases

with reducing D, ranging from $g = 0.083$ eV for the largest gap ($D = 40$ a$_0$) to $g = 0.27$ eV for the smallest one ($D = 16$ a$_0$). Two examples of the fittings performed for gap sizes $D = 16$ a$_0$ (blue line, A $= 6.77$ eV $\cdot$ nm^2, $\Delta\omega_0 = 0.67$ eV) and $D = 40$ a$_0$ (red line, A $= 7.43$ eV $\cdot$ nm^2, $\Delta\omega_0 = 0.02$ eV) are illustrated in Figure S6b.

In the literature, several criteria have been adopted for the strong-coupling regime to be identified.[30] In brief, the less demanding criterion states that $g > (\gamma_{\mathrm{QE}} - \gamma_p)/4$ has to be fulfilled. Other criteria often used are $g > (\gamma_{\mathrm{QE}} + \gamma_p)/4$, or the more restrictive $g > (\gamma_{\mathrm{QE}} + \gamma_p)/2$. In our system, already for the largest separation between the MNPs, $D = 40$ a$_0$, the condition $g > (\gamma_{\mathrm{QE}} + \gamma_p)/4$ is satisfied, and the more restrictive $g > (\gamma_{\mathrm{QE}} + \gamma_p)/2$ is nearly satisfied. For all the gaps smaller than $D \leq 32$ a$_0$, the condition $g > (\gamma_{\mathrm{QE}} + \gamma_p)/2$ is fulfilled.

To show more clearly that the resonant QE–MNPs system is in the strong-coupling regime, once the values of the coupling strength g are determined, we can calculate the energies of the upper (ω_+) and the lower (ω_-) polaritons for different values of the QE exciton energy ω_0 according to[31]

$$\omega_{\pm} = \frac{1}{2}(\omega_{\mathrm{BDP}} + \omega_0 - \Delta\omega) \pm \frac{1}{2}\mathrm{Re}\left\{\sqrt{4g^2 + \left[\omega_{\mathrm{BDP}} - (\omega_0 - \Delta\omega) + i\frac{\gamma_{\mathrm{QE}} - \gamma_{\mathrm{P}}}{2}\right]^2}\right\}, \tag{S41}$$

where Re{ } stands for the real part.

In Figures S6c-d, we show the values of ω_+ and ω_- as a function of the QE exciton energy ω_0 by white dashed lines, overlayed on the color maps of the absorption cross section, $\sigma_{\mathrm{abs}}(\omega)$, calculated for the smallest ($D = 16$ a$_0$, panel c) and largest ($D = 40$ a$_0$, panel d) values of the gap size considered in this work. For both gap separations, ω_+ and ω_- follow quite closely the maxima of the absorption, with the exception of the results obtained for high frequencies of the incident plane wave $\omega > 3.25$ eV, where high-order plasmonic modes (not accounted in the present coupled-oscillator model) influence the

results. The good agreement between the polaritonic energies $\omega_{\pm}$ and the resonances of $\sigma_{\text{abs}}(\omega)$ indicates that the absorption resonances calculated with classical electrodynamics simulations can be indeed identified as the polaritonic modes. Crucially, we obtain a well-resolved avoided crossing between the absorption resonances as well as between the upper (ω_+) and lower (ω_-) polaritons. Thus, at the avoided crossing between the calculated absorption resonances (at $\omega \approx \omega_{\text{BDP}} \approx \omega_0 - \Delta\omega$), the energy difference can be related to a good approximation with $2g$, which increases as the gap size is reduced. These results thus clearly indicate that the resonant QE–MNPs system described within the framework of classical electromagnetism is in the strong-coupling regime.

S5 Confirming the role of the electronic QE–MNPs coupling: a *semiclassical* approach

In this section, we apply a *semiclassical* approach to the QE–MNPs system in order to gain a better understanding of the role played by the electronic QE–MNPs coupling in the optical response. We consider here the same system as in the main text, consisting of a QE with a transition energy ω_0 located at the center of the nanogap formed by two Na nanoparticles of radius $R_{\text{MNP}} = 34.4$ a$_0$. We analyze the off-resonant ($\omega_0 = 2.58$ eV and $\omega_0 = 2.75$ eV) and the resonant ($\omega_0 = 2.95$ eV) cases.

Our *semiclassical* approach is based on the Green's function formalism (see Subsection S3.2), where the QE is introduced as a classical point dipole. The dipole moments induced at the MNPs and at the QE are then obtained from Equations S35. In contrast with a fully classical approach, however, the quantities $\hat{\mathbb{G}}(\mathbf{r}_{\text{QE}}, \mathbf{r}_{\text{QE}}, \omega)$, $\mathbf{E}^{\text{ind}}(\mathbf{r} = \mathbf{r}_{\text{QE}}, \omega)$, $\hat{\alpha}_{\text{dimer}}(\omega)$ and $\hat{\alpha}^{\text{QE}}_{\text{dimer}}(\omega)$ are obtained from the TDDFT simulations of the metallic dimer. To that end, we use the (real-time) linear-response TDDFT scheme following the procedure reported in refs. 2 and 24. Thus, this *semiclassical* approach, based on TDDFT calculations of the isolated dimer, naturally includes not only the nonlocality of the metals, but also other quantum

phenomena such as electron spill-out and finite-size effects inherent to the quantum nature of electrons. However, since the QE is introduced as a classical point dipole, the electronic coupling between the MNPs and the QE, as well as the actual electronic structure of the QE and the finite-size extension of its transition density are not accounted for. The comparison between the results obtained from fully TDDFT, *semiclassical*, and classical calculations thus provides deeper insight into the effect of the electronic QE–MNPs coupling on the optical absorption and allows us to discard nonlocal and finite-size effects as the source of QE exciton quenching. Therefore, this analysis further confirms the conclusions discussed in the main text.

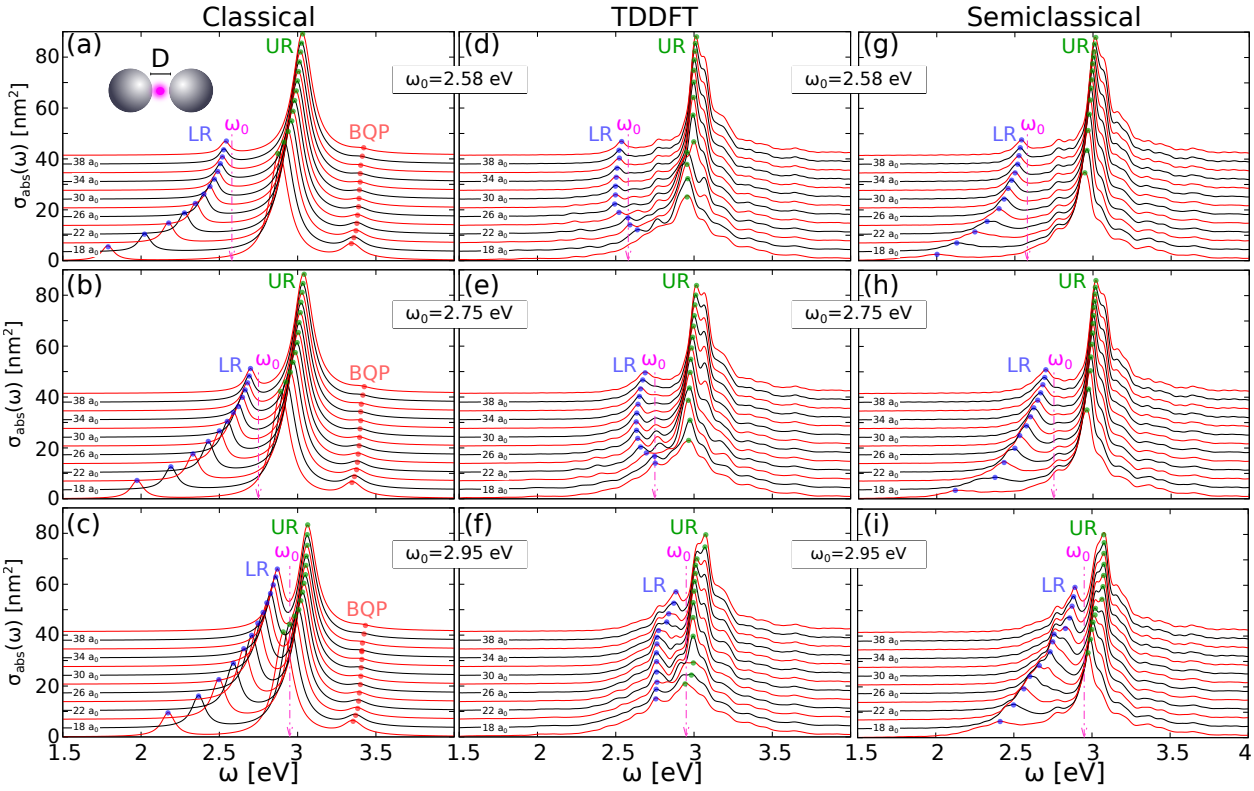

Figure S7: Waterfall plots of the optical absorption spectra of the coupled QE–MNPs system for a gap sizes ranging from $D = 16$ a$_0$ to $D = 40$ a$_0$ in steps of 2 a$_0$ (larger D on top). Results are shown as a function of frequency, ω, of an incident electromagnetic plane wave polarized along the dimer axis (z-axis). The value of D is indicated at each second spectra marked by the black lines. The results are obtained from **(a)-(c)** classical calculations, **(d)-(f)** TDDFT simulations, and the **(g)-(h)** *semiclassical* approach as described in this section. The resonant energies ω_0 of the isolated QE are marked with vertical magenta arrows, with $\omega_0 = 2.58$ eV for **(a)**,**(d)**,**(g)**, $\omega_0 = 2.75$ eV for **(b)**,**(e)**,**(h)**, and $\omega_0 = 2.95$ eV for **(c)**,**(f)**,**(i)**. The blue (lower resonance, LR), green (upper resonance, UR), and red (bonding quadrupolar plasmon, BQP) dots indicate the main modes of the system.

In Figure S7 we compare the optical absorption spectra of the coupled QE–MNPs system as obtained from the classical (left-side panels), the TDDFT (middle panels) and the *semiclassical* (right-side panels) approaches. Results are shown as waterfall plots for different values of the gap separation D and for three different resonant energies of the isolated QE, $\omega_0 = 2.58$ eV, 2.75 eV and 2.95 eV, as indicated in each panel (see Section S1). Using different values of ω_0 allows us to analyze the effect of the electronic QE–MNPs coupling in different scenarios where the QE is either in resonance ($\omega_0 = 2.95$ eV) or out of resonance ($\omega_0 = 2.58$ eV and $\omega_0 = 2.75$ eV) with the dominant BDP mode of the metallic dimer. The lower (LR) and upper (UR) resonances are marked with blue and green dots, respectively.

The differences observed between the classical (panels a–c) and the TDDFT (panels d–f) results are discussed in detail in Section S4 for the resonant case, $\omega_0 = 2.95$ eV, and in the main text for the off-resonant case, $\omega_0 = 2.58$ eV. This latter discussion also applies for the situation where $\omega_0 = 2.75$ eV, which shows qualitatively similar trends. Thus, we focus below on analyzing the differences between the *semiclassical* and the TDDFT absorption spectra for the three exciton energies.

For large distance between the MNPs, $D \sim 30 - 40$ a_0, the *semiclassical* (panels g, h and i) and TDDFT (panels d, e and f) results show very good agreement for the three QE exciton energies considered here. In particular, as discussed in Section S4 for the resonant case $\omega_0 = 2.95$ eV, the LR calculated with TDDFT (panel f) and the *semiclassical* model (panel i) is considerably weaker than that predicted by the classical approach (panel c). Thus, the *semiclassical* calculation indicates that the origin of the difference between the TDDFT and the classical absorption spectra resides on quantum phenomena such as nonlocality and finite-size effects that are important for such small metallic nanoparticles. Indeed, at large D there is no hybridization between the electronic states localized at the QE and at the MNPs.

For D below $D \sim 26$ a_0, the electronic QE–MNPs coupling affects the absorption

spectra of the system as follows from the comparison between the *semiclassical* and TDDFT results in Figure S7. First, the TDDFT shows substantial broadening and reduction of the amplitude for the UR evolving from the BDP of the nanoparticle dimer. These effects, not captured by the *semiclassical* model, are attributed to the charge-transfer processes between the MNPs. In our system, electron transport can occur at larger gap separations as compared to typical vacuum junctions because it is assisted by photoexcited electron transfer through the LUMO of the QE.[32]

However, the most spectacular effect of the electronic coupling is revealed by the LR mode, as already emphasized in the main text of the paper. In a similar manner as the classical approach, the *semiclassical* model also predicts a continuous redshift of the LR for the off-resonant cases (panels a–b and g–h), and increasing LR–UR splitting for the resonant case (panels c and i) with decreasing gap size D. As compared to classical results, the main difference is that the *semiclassical* model shows a weakening and a broadening of the LR upon decreasing D, which points toward nonlocal optical effects that can also affect the electromagnetic response for such a small system.[33] In sheer contrast, the TDDT calculations reveal smaller LR–UR splitting (panel f) for decreasing D and a blueshift of the LR (panels d and e) for $D \leq 26$ a_0, with a progressive merging of the LR and UR modes into a broad resonance structure. These effects are thus only observed when the hybridization between the MNPs and the QE electronic orbitals is possible (as it is naturally the case for the TDDFT), i.e., when the (excited) electron can tunnel across the system.

S6 Charge-Transfer Resonances at Low Energies

In Figure S8, we show the study of the charge-transfer resonances of the coupled QE–MNPs system for an incident field corresponding to z-polarized light oscillating in the low-frequency range $\omega = 0 - 1$ eV. The results in Figure S8a are the same as those shown in Figure 4 of the main text, where the QE is characterized by $R_{\mathrm{qe}} = 5$ a$_0$ and a background QE potential $V_0 = 1$ eV ($\omega_0 = 2.58$ eV, $\alpha_0 = 1.7$ au). In Figure S8b,c we show the results obtained for $V_0 = 3$ eV ($\omega_0 = 2.75$ eV, $\alpha_0 = 1.62$ au) and $V_0 = 5$ eV ($\omega_0 = 2.95$ eV, $\alpha_0 = 1.52$ au), respectively. Thus, our analysis is extended to cases where

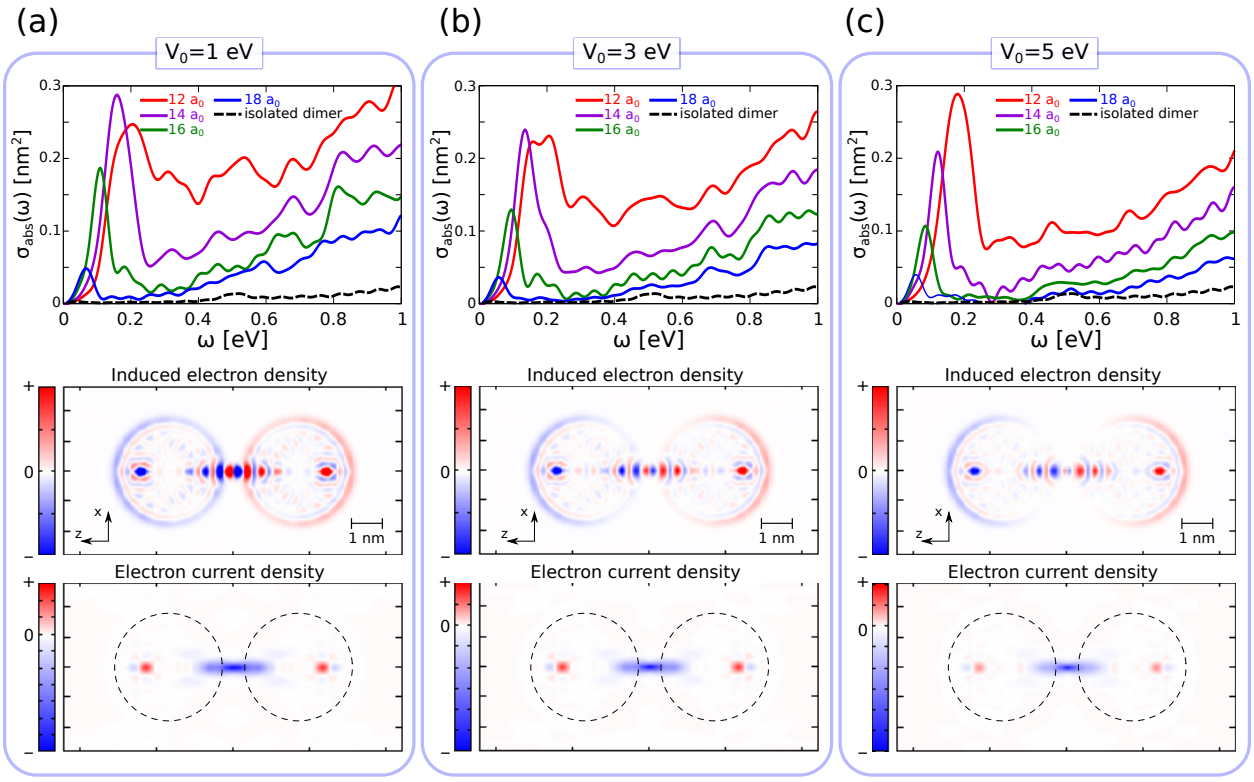

Figure S8: Study of the charge-transfer resonances of the coupled QE–MNPs system for low illumination frequencies $\omega = 0 - 1$ eV. Results are shown for three different background QE potentials, **(a)** $V_0 = 1$ eV, **(b)** $V_0 = 3$ eV, and **(c)** $V_0 = 5$ eV. The incident electromagnetic plane wave is polarized along the dimer axis (z-axis). Upper panels: absorption spectra for a gap separation D ranging from $D = 12$ a$_0$ to $D = 18$ a$_0$, as indicated in the insets. The reference absorption spectrum of the isolated metallic dimer for $D = 12$ a$_0$ is shown by the dashed black line. Lower panels: induced electron density and electron-current density along the z-direction at the charge-transfer frequency ω_{CT}. The gap separation is $D = 16$ a$_0$. The snapshots are taken at the instants of time when the total dipole moment (induced density maps) and the electron-current density (current density maps) at the middle of the junction are maximum. The color code is explained in the insets.

the isolated QE is characterized by different values of the oscillator strength and transition frequency (see Table S1). As observed in Figure S8, the present QE–MNPs system exhibits qualitatively similar charge-transfer resonances regardless of the specific characteristics of the QE (within the range of their variation encompassed here). This points at similar electron-transport properties of the QE–MNPs coupled junction.

References

[S1] Szabo, A.; Ostlund, N. S. Modern quantum chemistry: introduction to advanced electronic structure theory; Courier Corporation, 2012.

[S2] Marinica, D.; Kazansky, A.; Nordlander, P.; Aizpurua, J.; Borisov, A. G. Quantum Plasmonics: Nonlinear Effects in the Field Enhancement of a Plasmonic Nanoparticle Dimer. Nano Letters **2012**, 12, 1333–1339.

[S3] Perdew, J. P.; Tran, H. Q.; Smith, E. D. Stabilized jellium: Structureless pseudopotential model for the cohesive and surface properties of metals. Phys. Rev. B **1990**, 42, 11627–11636.

[S4] Marinica, D. C.; Zapata, M.; Nordlander, P.; Kazansky, A. K.; Echenique, P. M.; Aizpurua, J.; Borisov, A. G. Active quantum plasmonics. Science advances **2015**, 1, e1501095.

[S5] Aguirregabiria, G.; Marinica, D. C.; Esteban, R.; Kazansky, A. K.; Aizpurua, J.; Borisov, A. G. Electric Field-Induced High Order Nonlinearity in Plasmonic Nanoparticles Retrieved with Time-Dependent Density Functional Theory. ACS Photonics **2017**, 4, 613–620.

[S6] Aguirregabiria, G.; Marinica, D.-C.; Ludwig, M.; Brida, D.; Leitenstorfer, A.; Aizpurua, J.; Borisov, A. G. Dynamics of electron-emission currents in plasmonic gaps induced by strong fields. Faraday discussions **2019**, 214, 147–157.

[S7] Yabana, K.; Bertsch, G. Time-dependent local-density approximation in real time. Physical Review B **1996**, 54, 4484.

[S8] Carminati, R.; Greffet, J.-J.; Henkel, C.; Vigoureux, J. Radiative and non-radiative decay of a single molecule close to a metallic nanoparticle. Optics Communications **2006**, 261, 368 – 375.

[S9] Anger, P.; Bharadwaj, P.; Novotny, L. Enhancement and Quenching of Single-Molecule Fluorescence. Phys. Rev. Lett. **2006**, 96, 113002.

[S10] Savin, A.; Umrigar, C. J.; Gonze, X. Relationship of Kohn–Sham eigenvalues to excitation energies. Chemical Physics Letters **1998**, 288, 391–395.

[S11] Onida, G.; Reining, L.; Rubio, A. Electronic excitations: density-functional versus many-body Green's-function approaches. Reviews of modern physics **2002**, 74, 601.

[S12] Vignale, G.; Kohn, W. Current-Dependent Exchange-Correlation Potential for Dynamical Linear Response Theory. Phys. Rev. Lett. **1996**, 77, 2037–2040.

[S13] Wijewardane, H. O.; Ullrich, C. A. Time-Dependent Kohn-Sham Theory with Memory. Phys. Rev. Lett. **2005**, 95, 086401.

[S14] Gunnarsson, O.; Lundqvist, B. I. Exchange and correlation in atoms, molecules, and solids by the spin-density-functional formalism. Physical Review B **1976**, 13, 4274.

[S15] Chulkov, E.; Borisov, A.; Gauyacq, J.; Sánchez-Portal, D.; Silkin, V.; Zhukov, V.; Echenique, P. Electronic excitations in metals and at metal surfaces. Chemical Reviews **2006**, 106, 4160–4206.

[S16] Zugarramurdi, A.; Zabala, N.; Chulkov, E. Electronic structure, dynamics and spectroscopy of metallic nanosized systems: Pb thin overlayers and Na nanocontacts. Ph.D. thesis, 2011.

[S17] Schmeits, M. Surface-plasmon coupling in cylindrical pores. Physical Review B **1989**, 39, 7567.

[S18] Schmeits, M.; Dambly, L. Fast-electron scattering by bispherical surface-plasmon modes. Physical review B **1991**, 44, 12706.

[S19] Teperik, T. V.; Nordlander, P.; Aizpurua, J.; Borisov, A. G. Robust subnanometric plasmon ruler by rescaling of the nonlocal optical response. Physical review letters **2013**, 110, 263901.

[S20] Luo, Y.; Fernandez-Dominguez, A.; Wiener, A.; Maier, S. A.; Pendry, J. Surface plasmons and nonlocality: a simple model. Physical review letters **2013**, 111, 093901.

[S21] Toscano, G.; Straubel, J.; Kwiatkowski, A.; Rockstuhl, C.; Evers, F.; Xu, H.; Mortensen, N. A.; Wubs, M. Resonance shifts and spill-out effects in self-consistent hydrodynamic nanoplasmonics. Nature communications **2015**, 6, 7132.

[S22] Teperik, T. V.; Nordlander, P.; Aizpurua, J.; Borisov, A. G. Quantum effects and nonlocality in strongly coupled plasmonic nanowire dimers. Optics express **2013**, 21, 27306–27325.

[S23] Novotny, L.; Hecht, B. Principles of nano-optics; Cambridge university press, 2012.

[S24] Babaze, A.; Esteban, R.; Aizpurua, J.; Borisov, A. G. Second-Harmonic Generation from a Quantum Emitter Coupled to a Metallic Nanoantenna. ACS Photonics **2020**, 7, 701–713.

[S25] Carmina Monreal, R.; Antosiewicz, T. J.; Peter Apell, S. Competition between surface screening and size quantization for surface plasmons in nanoparticles. New Journal of Physics **2013**, 15, 083044.

[S26] Baida, H.; Billaud, P.; Marhaba, S.; Christofilos, D.; Cottancin, E.; Crut, A.; Lermé, J.; Maioli, P.; Pellarin, M.; Broyer, M.; Del Fatti, N.; Vallée, F.; Sánchez-Iglesias, A.; Pastoriza-Santos, I.; Liz-Marzán, L. M. Quantitative Determination of the Size Dependence of Surface Plasmon Resonance Damping in Single Ag@SiO2 Nanoparticles. Nano Letters **2009**, 9, 3463–3469, PMID: 19719148.

[S27] Aizpurua, J.; Borisov, A. World Scientific Handbook of Metamaterials and Plasmonics; World Scientific, 2017; Vol. 4; Chapter 4.

[S28] Romero, I.; Aizpurua, J.; Bryant, G. W.; de Abajo, F. J. G. Plasmons in nearly touching metallic nanoparticles: singular response in the limit of touching dimers. Opt. Express **2006**, 14, 9988–9999.

[S29] Rossi, T. P.; Shegai, T.; Erhart, P.; Antosiewicz, T. J. Strong plasmon-molecule coupling at the nanoscale revealed by first-principles modeling. Nature communications **2019**, 10, 3336.

[S30] Törmä, P.; Barnes, W. L. Strong coupling between surface plasmon polaritons and emitters: a review. Reports on Progress in Physics **2014**, 78, 013901.

[S31] Autore, M.; Li, P.; Dolado, I.; Alfaro-Mozaz, F. J.; Esteban, R.; Atxabal, A.; Casanova, F.; Hueso, L. E.; Alonso-González, P.; Aizpurua, J.; Nikitin, A. Y.; Vélez, S.; Hillenbrand, R. Boron nitride nanoresonators for phonon-enhanced molecular vibrational spectroscopy at the strong coupling limit. Light: Science & Applications **2018**, 7, 17172–17172.

[S32] Marinica, D. C.; Silkin, V. M.; Kazansky, A. K.; Borisov, A. G. Controlling gap plasmons with quantum resonances. Physical Review B **2018**, 98, 155426.

[S33] Ciracì, C.; Jurga, R.; Khalid, M.; Della Sala, F. Plasmonic quantum effects on single-emitter strong coupling. Nanophotonics **2019**, 8, 1821–1833.